Image quality improvement of a one-step spectral CT reconstruction on a prototype photon-counting scanner

Pierre-Antoine Rodesch, Salim Si-Mohamed, Jérôme Lesaint, Philippe Douek, Simon Rit

▶ **To cite this version:**

Pierre-Antoine Rodesch, Salim Si-Mohamed, Jérôme Lesaint, Philippe Douek, Simon Rit. Image quality improvement of a one-step spectral CT reconstruction on a prototype photon-counting scanner. Physics in Medicine and Biology, 2023, 69 (1), pp.015005. 10.1088/1361-6560/ad11a3 . hal-04362389

HAL Id: hal-04362389
https://hal.science/hal-04362389v1

Submitted on 22 Dec 2023

HAL is a multi-disciplinary open access archive for the deposit and dissemination of scientific research documents, whether they are published or not. The documents may come from teaching and research institutions in France or abroad, or from public or private research centers.

L'archive ouverte pluridisciplinaire **HAL**, est destinée au dépôt et à la diffusion de documents scientifiques de niveau recherche, publiés ou non, émanant des établissements d'enseignement et de recherche français ou étrangers, des laboratoires publics ou privés.

Distributed under a Creative Commons Attribution - NonCommercial 4.0 International License

Image quality improvement of a one-step spectral CT reconstruction on a prototype photon-counting scanner

Pierre-Antoine Rodesch[1], Salim A. Si-Mohamed[1,2], Jérôme Lesaint[1], Philippe C. Douek[1,2], Simon Rit[1]

[1] University of Lyon, CREATIS, CNRS UMR5220, Inserm U1294, INSA-Lyon, Université Lyon 1, Centre Léon Bérard, France

[2] Department of Radiology, Louis Pradel Hospital, Hospices Civils de Lyon, Bron, France

E-mail: pierreantoine.rodesch@gmail.com

July 2023

Abstract. *Objective.* X-ray spectral computed tomography (CT) allows for material decomposition (MD). This study compared a one-step material decomposition MD algorithm with a two-step reconstruction MD algorithm using acquisitions of a prototype CT scanner with a photon-counting detector (PCD). *Approach.* MD and CT reconstruction may be done in two successive steps, i.e. decompose the data in material sinograms which are then reconstructed in material CT images, or jointly in a one-step algorithm. The one-step algorithm reconstructed material CT images by maximizing their Poisson log-likelihood in the projection domain with a spatial regularization in the image domain. The two-step algorithm maximized first the Poisson log-likelihood without regularization to decompose the data in material sinograms. These sinograms were then reconstructed into material CT images by least squares minimization, with the same spatial regularization as the one step algorithm. A phantom simulating the CT angiography clinical task was scanned and the data used to measure noise and spatial resolution properties. Low dose carotid CT angiographies of 4 patients were also reconstructed with both algorithms and analyzed by a radiologist. The image quality and diagnostic clinical task were evaluated with a clinical score. *Main results.* The phantom data processing demonstrated that the one-step algorithm had a better spatial resolution at the same noise level or a decreased noise value at matching spatial resolution. Regularization parameters leading to a fair comparison were selected for the patient data reconstruction. On the patient images, the one-step images received higher scores compared to the two-step algorithm for image quality and diagnostic. *Significance.* Both phantom and patient data demonstrated how a one-step algorithm improves spectral CT image quality over the implemented two-step algorithm but requires a longer computation time. At a low radiation dose, the one-step algorithm presented good to excellent clinical scores for all the spectral CT images.

Keywords: Computed tomography, spectral CT, photon-counting detector, material decomposition, image quality, one-step

1. Introduction

Photon-counting detector computed tomography (PCD-CT) represents a milestone in medical imaging (Danielsson *et al.* 2021; Si-Mohamed *et al.* 2021b; Rajendran *et al.* 2021). Compared to energy-integrating detectors (EIDs), PCDs improve the spatial resolution for the same dose level and enable low-dose clinical protocols. These improvements have been demonstrated with conventional images, i.e. the CT image reconstructed from the attenuation of all detected photons. The conventional image is traditionally reconstructed with filtered back-projection (FBP) for EID-CT and PCD-CT. The improved resolution and noise properties come from the detection technology.

PCDs and dual-energy (DE) EIDs also provide spectral images (McCollough *et al.* 2020) but spectral images inherently suffer from a higher noise level than conventional imaging. While the reconstruction algorithm is rather similar between CT systems in conventional imaging, different strategies have been adopted to reconstruct the spectral images and fundamentally different algorithms have been developed.

Spectral x-ray images measure the energy variability of the attenuation coefficient of the patient. In most cases, spectral CT uses the model of Alvarez and Macovski 1976 which describes the variations of the linear attenuation coefficients with energy by the linear combination of a few basis functions. With this model, the reconstruction of the energy-resolved CT image of a patient comes down to the reconstruction of two basis material CT images (with an additional basis material CT image for each K-edge contrast agent). This material decomposition (MD) formulation combined with a multi-energy measurement (performed either with a DE-CT or a PCD-CT scanner) enables material identification and quantification.

In PCD-CT acquisitions, several thresholds are set to define a corresponding set of energy bins, each photon detected by the detector being sorted in the bin corresponding to its measured energy. Because of physical phenomena in the detector (charge sharing, fluorescence escape, etc.), the PCD spectral response is imperfect (Flohr *et al.* 2020; Si-Mohamed *et al.* 2021b) which has to be taken into account in the reconstruction. The spectral distortion is often accounted for during MD. MD and tomographic reconstruction are the two sub-problems of spectral CT reconstruction.

Different strategies have been developed to tackle spectral CT reconstruction. They can be classified into three categories depending on when MD occurs: pre-, post- or during tomographic reconstruction. Pre-reconstruction techniques perform a projection-based MD: basis sinograms are first decomposed from the energy bins (Roessl and Proksa 2007) and then reconstructed into basis CT images. These methods are computationally efficient but it is difficult to implement noise reduction techniques in projection space and crucial statistical information is lost after MD. Post-reconstruction techniques first reconstruct the CT image of each energy bin (Maaß *et al.* 2009). However, these reconstructed CT images suffer from beam-hardening artifacts which will degrade the accuracy of the post-reconstruction MD. Finally, one-step (or joint) reconstruction performs the MD and the tomographic reconstruction jointly. They directly reconstruct

the basis material volumes from the multi-energy projection measurements, unlike pre- and post-reconstruction techniques which have multiple steps with intermediate results.

All one-step algorithms are iterative unlike pre- and post-reconstruction methods which can use FBP for tomographic reconstruction. One advantage is that spatial regularization of the material CT images may be used while performing the MD. However, these techniques are computationally more demanding and require an efficient optimization algorithm. Several algorithms have been investigated for one-step reconstruction: non-linear conjugate gradient (Cai *et al.* 2013; Simard and Bouchard 2022), separable quadratic surrogates (SQS) (Lee *et al.* 2022; Liu *et al.* 2022; Long and Fessler 2014; Mechlem *et al.* 2017; Tilley *et al.* 2019; Weidinger *et al.* 2016) or algorithms based on *proximal* operators such as ADMM (Jolivet *et al.* 2020; Schmidt *et al.* 2022), Chambolle-Pock (Barber *et al.* 2016; Chen *et al.* 2021) or VMILa (Tairi *et al.* 2020). A previous comparative study (Mory *et al.* 2018) has demonstrated that SQS combined with Nesterov's momentum is an efficient algorithm.

This study aimed at demonstrating the image quality improvement of one-step approaches over a pre-reconstruction MD method, called two-step in the following. Existing one-step algorithms have been compared to two-step methods (Mechlem *et al.* 2017; Simard and Bouchard 2022) but, to our knowledge, no study has rigorously compared the image quality of one-step and two-step material decomposition strategies. In this study, a one-step algorithm and a two-step algorithm were selected from the literature and implemented. Aiming at a comparison as fair as possible, the two-step method uses iterative tomographic reconstruction with the same spatial regularization as the one-step method. In a similar study limited to simulated data, one-step reconstruction has already demonstrated its potential to reduce metal artifacts compared to a two-step method (Schmidt *et al.* 2022). Here, experimental data acquired with a full field-of-view (FOV) (500 mm) clinical prototype PCD-CT are used (Si-Mohamed *et al.* 2023). We propose a methodology to select the hyperparameters of model-based algorithms from empirical measurements leading to a fair comparison of both methods before applying it to patient data. Only a few one-step methods have been applied to patient data and this study demonstrates that they can facilitate the diagnosis on spectral images.

The first part of this work investigates different regularization strengths for the two methods to select parameters yielding the same level of noise or the same spatial resolution. Image quality metrics are then evaluated and compared. In a second part of this work, patient data were reconstructed and analyzed by radiologists for a specific clinical task: carotid angiography.

2. Material and Methods

2.1. Spectral forward model

The same forward spectral model was inverted in the two-step or one-step methods for MD. This model estimates the photon count $\overline{C}_{ib}$ in the energy bin b at the detector pixel i from the scanned object attenuation:

$$\overline{C}_{ib} = \int_{T^b_{\min}}^{T^b_{\max}} \int_0^{\mathrm{kVp}} S^{\mathrm{Resp}}(t,e) e^{-\mathrm{att}_i(e)} \mathrm{d}e \, \mathrm{d}t \tag{1}$$

where $T^b_{\min}$ and $T^b_{\max}$ are respectively the lower and upper thresholds defining the energy bin b, kVp is the tube voltage value, S^{Resp} the spectral response, and att_i the attenuation. The spectral response includes the PCD response and the incident source spectrum.

In the following, a discretized notation of this model is used where the spectral response is a discretized spectrum per bin:

$$\overline{C}_{ib} \simeq \sum_{e=1}^{\mathrm{kVp}} S^{\mathrm{Resp}}_{be} e^{-\mathrm{att}_{ie}}. \tag{2}$$

This forward model is based on the assumption that the PCD behavior is linear. Non-linearities such as pile-up effects or scatter are neglected. It also relies on an accurate knowledge of the spectral response, in order to avoid low and high frequency artifacts (Feng *et al.* 2021).

Using the model of Alvarez and Macovski 1976, the attenuation is decomposed into several basis material lengths in the two-step method:

$$\mathrm{att}^{\mathrm{TS}}_{ie} = \sum_{m=1}^{N_m} l_{im} \mu_{me} \tag{3}$$

where N_m is the number of basis materials, l is the concatenated vector representing the basis material sinograms (with m the material index) and μ_{me} the attenuation coefficient of the basis material.

For the one-step method, the attenuation is decomposed into several basis material densities:

$$\mathrm{att}^{\mathrm{OS}}_{ie} = \sum_{m=1}^{N_m} [A f_m]_i \mu_{me} \tag{4}$$

where f is the concatenated vector representing the basis material volumes and A is the projection matrix to compute a material sinogram from a material volume f_m.

2.2. Two-step method

The two-step MD was implemented in a projection-based scheme (Roessl and Proksa 2007) which computes in a first step the material sinograms from the PCD data

by maximizing pixel by pixel the Poisson log-likelihood of measuring c_{ib} counts after traversing l_i lengths of materials:

$$\mathrm{PL}^{\mathrm{TS}}(l_i) = \sum_{b=1}^{N_b} \left[c_{ib} \log\left(\overline{C}_{ib}^{\mathrm{TS}}(l_i)\right) - \overline{C}_{ib}^{\mathrm{TS}}(l_i) \right] \tag{5}$$

where

$$\overline{C}_{ib}^{\mathrm{TS}}(l_i) = \sum_{e=1}^{\mathrm{kVp}} S_{be}^{\mathrm{Resp}} \exp\left(- \sum_{m=1}^{N_m} l_{im} \mu_{me} \right) \tag{6}$$

combines eq. (2) and (3). Given the pixel by pixel formulation, this log-likelihood is a function of N_m scalars and is a small optimization problem (N_m being equal to 2 in this work). The argument of the maximum was computed with the Nelder-Mead downhill simplex algorithm (Nelder and Mead 1965).

In a second step, the basis material sinograms were used independently as input of a conjugate gradient (CG) algorithm (Nocedal 2006) minimizing the penalized least-square difference between the decomposed sinograms and the projections of the reconstructed material map:

$$\mathrm{PLS}(f_m) = \sum_{i=1}^{N_p} ||A f_m - l_m||^2 + \lambda_m^{\mathrm{TS}} R(f_m) \tag{7}$$

where N_p is the number of detector pixels, $R(f_m)$ is a spatial regularization term and λ_m^{TS} is the regularization weight defined for each basis material. The spatial regularization is defined by:

$$R(f_m) = \sum_{j=1}^{N_v} \sum_{\xi \in \mathrm{N_j}} \phi(f_{mj} - f_{m\xi}) \tag{8}$$

where j is the voxel index, N_v is the number of voxels in the material volume and $\mathrm{N_j}$ is the set of neighbouring voxels of the j-th voxel. In this study, ϕ is the Green prior function (Green 1990) which approximates the absolute value function and is twice differentiable:

$$\phi(x) = \frac{27}{128} \log\left[\cosh\left(\frac{16}{3\sqrt{3}} x \right) \right]. \tag{9}$$

2.3. One-step method

The one-step method reconstructs directly the material volumes from the measured counts. The implemented method also used the Poisson log-likelihood as in eq. (5) but as a function of the material volumes f:

$$\mathrm{PL}^{\mathrm{OS}}(f) = \sum_{i=1}^{N_p} \sum_{b=1}^{N_b} \left[c_{ib} \log\left(\overline{C}_{ib}^{\mathrm{OS}}(f)\right) - \overline{C}_{ib}^{\mathrm{OS}}(f) \right] - \sum_{m=1}^{N_m} \lambda_m^{\mathrm{OS}} R(f_m) \tag{10}$$

where

$$\overline{C}_{ib}^{\mathrm{OS}}(f) = \sum_{e=1}^{\mathrm{kVp}} S_{be}^{\mathrm{Resp}} \exp\left(- \sum_{m=1}^{N_m} [A f_m]_i \mu_{me} \right) \tag{11}$$

combines eq. (2) and (4) and $R(f_m)$ is the same regularization term as in eq. (8) with λ_m^{OS} the associated weights. Since the material volumes are jointly reconstructed, the regularization of one material map will impact the others. In contrast, the two-step algorithm reconstructs each material map independently and the regularization of one volume will not impact the others. This is a crucial difference between the two techniques which was accounted for in the following when adjusting the regularization parameters λ_m^{TS} and λ_m^{OS}.

The Poisson log-likelihood was maximized using the SQS-based algorithm developed by Weidinger *et al.* 2016 with two modifications to accelerate the convergence, the use of ordered subsets (Hudson and Larkin 1994) and of Nesterov's momentum technique (Nesterov 2005). The projections were randomly sorted into 8 subsets and Nesterov's momentum was reset every 50 iterations (i.e. every 400 updates). Finally, the one-step method may be unstable at the superior and inferior ends of the CT image. We used the correction described by Rodesch *et al.* 2020 based on spatial regularization weights. This method increases the spatial regularization at the superior and inferior extremities where each voxel is seen by fewer projection pixels.

2.4. PCD-CT scanner

The two-step and one-step methods were implemented within the Reconstruction Toolkit (RTK) (Rit *et al.* 2014) and tested on real data measured with a PCT-CT scanner (SPCCT, Philips Healthcare, Haifa, Israel). This pre-clinical prototype has a 500 mm FOV, a 1.825 magnification factor and a Z-coverage of 17.6 mm (Si-Mohamed *et al.* 2023). Projections were acquired with a 5 energy bins PCD-CT scanner. It was operated in a 2×2 binning mode, resulting in a 0.55 x 0.55 mm pixel size at the isocenter and 32×924 (binned) pixels per projection, in axial mode for the phantom acquisitions and in helical mode for the patient protocol. In both modes, 2400 projections per rotation were acquired but the source parameters were set to different values, as described in the following.

Prior to all acquisitions, images of a step wedge were acquired to calibrate the spectral response S^{Resp} (Eq. (2)) for the selected source parameters (voltage and current). This procedure has been developed by the system manufacturer. Additionally, a post-processing routine is also provided by the manufacturer to correct for concentric ring artifacts in the material density maps which was applied to all reconstructed images. The assumption is made that this correction equally affects the two-step and one-step images which was validated empirically.

2.5. Phantom geometry

A 100 mm diameter cylindrical module (figure 1) was placed in an anthropomorphic thorax phantom (QRM, Moehrendorf, Germany). This module was designed to reproduce the contrast of a coronary CT angiography (CTA) protocol. The thorax phantom simulates the attenuation of the chest of a small human adult and its

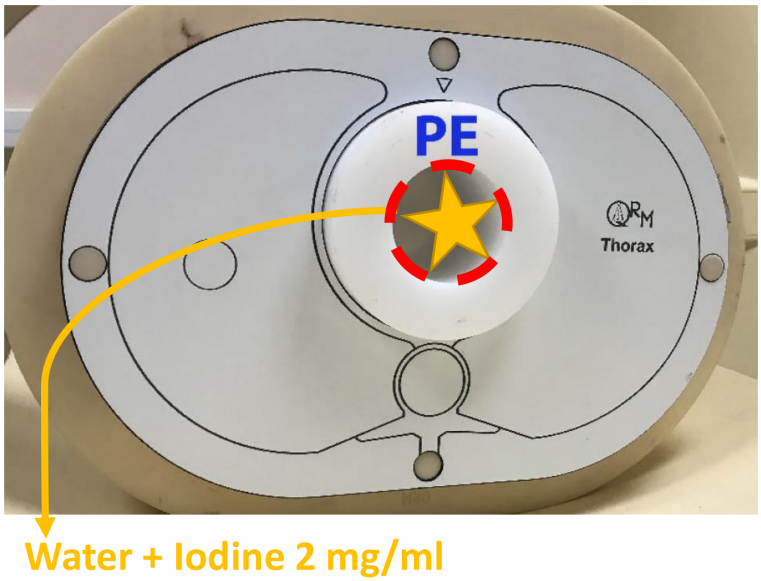

Figure 1. Photograph of the CTA module placed inside the QRM anthropomorphic thorax phantom.

height is 10 cm. The same phantom was used previously to compare the quality of PCD-CT conventional images with state-of-the-art DE-CT (Rotzinger *et al.* 2021). It is made of polyethylene (PE) with a 50 mm diameter hole, filled with iodine at 2 mg/ml concentration. The phantom was scanned with an axial protocol (rotation time: 1 s), a 120 kVp tube voltage and 80 mA current. The thresholds were set to 30/51/62/72/81 keV. MD CT images were reconstructed with both MD methods and a 0.25 x 0.25 x 0.5 mm voxel size. The reconstructed FOV was 500 x 500 x 10 mm.

2.6. Evaluation metrics

The PE and iodine have close densities in the water map (respectively 970 and 1020 mg/ml, see table 1). The contrast between the PE and the iodine, dominant

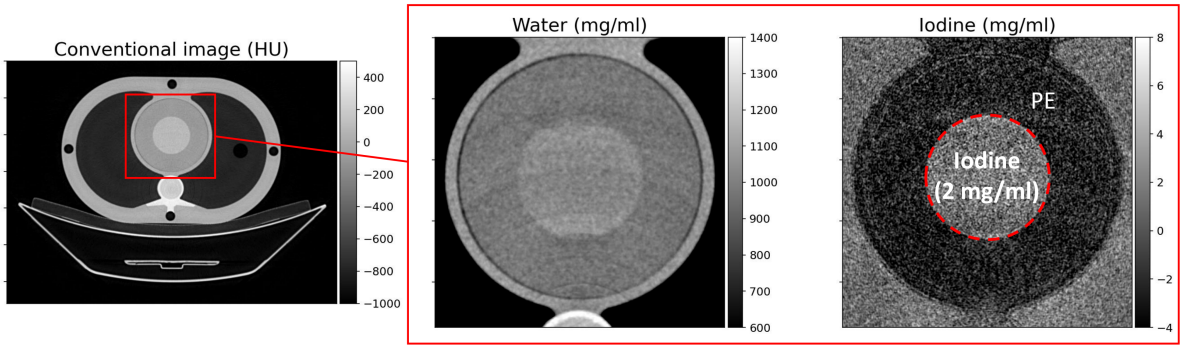

Figure 2. Left: conventional image of the anthropomorphic phantom. Right: water/iodine MD CT images of the CTA module. The dashed circle indicates the PE/iodine transition used for the assessment of the spatial resolution.

in the iodine CT image, is about 4 mg/ml. This corresponds to the CTA clinical task (see figure 2 and supplemental figure I). The water/iodine MD was computed for each method with various values of the regularization parameters. For each regularization parameter, the iodine concentration was measured in the iodine map. Additionally, the spatial resolution and the noise level were measured in both maps (water and iodine). They were evaluated individually for each slice and then averaged on 20 slices.

Table 1. Mean values of the PE and iodine solution measured in the conventional and the water/iodine MD CT images. HU numbers were measured in the conventional image reconstructed by the scanner manufacturer, the material densities were measured in the one-step case $(\lambda_{\mathrm{I}}^{\mathrm{OS}}, \lambda_{\mathrm{W}}^{\mathrm{OS}}) = (5000, 0.5)$

Material :	Conventional (HU)	Water map (mg/ml)	Iodine map (mg/ml)
PE	-90	+970	-2.0
Iodine	+95	+1020	+2.0

The iodine concentration was measured in a 50 mm diameter region-of-interest (ROI) at the center of the iodine insert. Thanks to the water/iodine MD, the voxel values of the iodine map directly provide the concentration of the iodine solution in mg/ml.

The spatial resolution was measured as the frequency corresponding to a task transfer function (TTF) value of 10% ($f_{\mathrm{TTF10\%}}$), evaluated on the PE/iodine transition (red dashed circle in figure 2) using the circular rod method (Samei *et al.* 2019). The edge spread function (ESF) was modeled by an error function to facilitate the TTF computation (Richard *et al.* 2012).

The noise level was measured in the iodine insert. A 90 mm diameter circular ROI was placed at the center of the iodine insert and the noise was measured with the standard deviation of the voxel intensities in the iodine module.

2.7. Comparison of three specific phantom cases

From the various reconstruction cases, each with a different set of regularization parameters as described in the next section, three were selected for further comparison: a two-step regularization level and two one-step combinations of regularization weights, providing either the same $f_{\mathrm{TTF10\%}}$ or the same noise level as the selected two-step case. The noise power spectrum (NPS) and the TTF curve in the iodine volume were evaluated for these three cases only. The TTF curve was derived from the fitted error function (Richard *et al.* 2012). For the NPS evaluation, a second order polynomial was fitted to the image and then subtracted from each slice to obtain a white noise image. The NPS was then evaluated from 64 x 64 voxels ROIs (Samei *et al.* 2019), with 10 ROIs per slice, resulting in a total of 200 ROIs.

2.8. Patient Data

Four patients underwent a routine low dose carotid CTA (mean age: 67.7 ± 7.7 years, body mass index: 23.5 ± 2.7 kg/m^2) with iodine contrast agent injection (Boccalini *et al.* 2021). The injected iodine contrast agent (Iomeprol, Iomeron 400, Bracco Imaging, Milan, Italy) concentration was 300 mg/ml. A volume of 40 ml was injected, followed by the injection of 20 ml of a saline solution. The system was operated with the same binning and threshold configuration as for the phantom acquisitions. The reconstructed voxel size was also set to the same value: 0.25 x 0.25 x 0.5 mm. The images were acquired with a 120 mm helical trajectory (pitch = 1.17), 0.33 s rotation time, 80 mA current and 120 kV tube voltage. This represents 25% of the normal dose for the recommended carotid CTA protocol.

The regularization parameter of the iodine image of the two-step method was selected to match the noise level of the iodine map in the clinical CTA protocol (Boccalini *et al.* 2021). Then a water/iodine MD was computed with both methods with the regularization parameters providing equivalent spatial resolution levels in the iodine map on the phantom data. From the reconstructed water/iodine MD CT images, virtual mono-energetic images (VMIs) were computed at 40, 50, 60, 70 and 80 keV. For the reconstruction of the water sinogram in the two-step method, different regularization levels were investigated. The water regularization parameter was set to a value providing a trade-off for the noise in the VMIs at the different energies.

One radiologist with 7 years of experience, blinded to image type and patient's identity, reviewed all images independently in a random order. Changes in image and window settings were allowed according to personal preferences. The reviewer scored the images independently using a 5-point quality score (1: insufficient, 5: excellent), according to different criteria defined in a prior work about coronary CTA (Si-Mohamed *et al.* 2022). Imaging quality criteria were assessed in all VMIs and the iodine image: overall quality, noise and sharpness. Additionally, three CCTA diagnostic tasks were evaluated in all VMIs: visualisation of vessel lumen, calcified and non calcified plaque (Leipsic *et al.* 2014; Weigold *et al.* 2011). In the iodine image, only one clinical task was assessed: the vessel lumen visualization. A patient's CT scan was considered of sufficient diagnostic quality if overall image quality score was higher than 3.

For comparison purposes, the overall mean score were computed and graphically displayed. An image per image improvement percentage was also computed.

3. Results

3.1. Spectral quantification

The accuracy and the convergence were assessed for each reconstruction. The measured iodine concentrations are presented in table 2 for various regularization parameters including extreme values.

The maximum iodine concentration deviation between two cases is 0.06 mg/ml,

Table 2. Iodine concentration (mg/ml)

	TS	OS $\lambda_W^{OS} = 0.0$	OS $\lambda_W^{OS} = 0.1$	OS $\lambda_W^{OS} = 0.5$	OS $\lambda_W^{OS} = 2.0$	
$\lambda_I^{TS} = 10$	1.99	1.96	1.97	1.98	1.98	$\lambda_I^{OS} = 1$
$\lambda_I^{TS} = 50$	2.00	1.97	1.98	1.98	1.98	$\lambda_I^{OS} = 1000$
$\lambda_I^{TS} = 100$	2.01	1.98	1.99	1.99	1.99	$\lambda_I^{OS} = 3000$
$\lambda_I^{TS} = 200$	2.02	2.00	2.00	2.00	2.00	$\lambda_I^{OS} = 6000$
$\lambda_I^{TS} = 300$	2.02	2.01	2.01	2.01	2.01	$\lambda_I^{OS} = 10000$

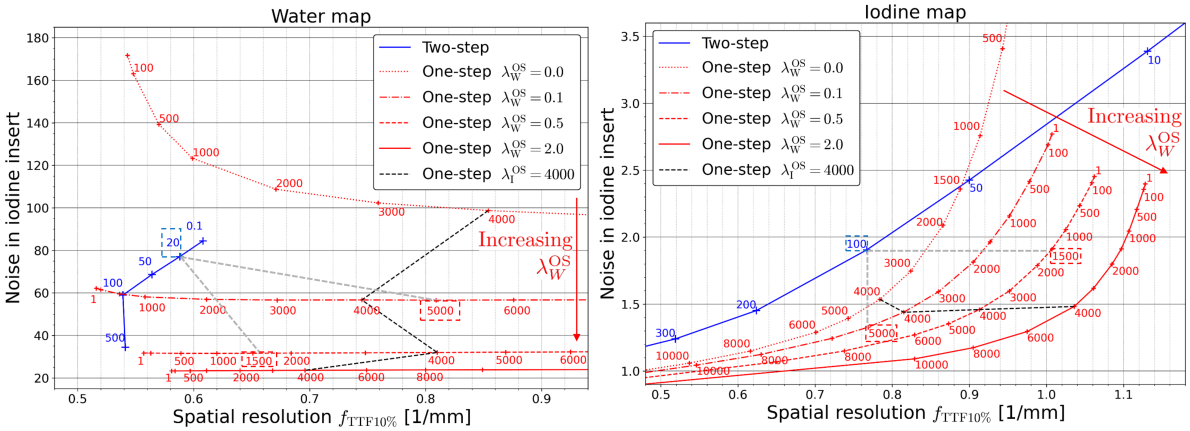

Figure 3. Noise/spatial resolution trade-off for various reconstructed cases with different values of the regularization parameters. The image quality improves with increasing abscissa and decreasing ordinates, i.e., towards the bottom right corners of the plots. The blue number attached to the data points of the blue curve are the two-step regularization weights. As the two-step reconstructions are independent, each blue point is only characterized by one value: the values displayed in the water map (left graph) are λ_W^{TS} and in the iodine map (right graph): λ_I^{TS}. The red points are representing each one-step reconstruction and each one is characterized by two values: λ_I^{OS} indicated as a red number in the graph and λ_W^{OS} in the legend. The cases squared in the plots were selected for further analysis.

corresponding to 3% of the theoretical value. This value is below the dilution accuracy and can be considered negligible. Based on past evaluations of one-step reconstruction Mory *et al.* 2018, this indicates that the different algorithms have reached convergence.

3.2. Regularization parameters

The trade-off between spatial resolution, measured with $f_{TTF10\%}$, and the noise level is presented for both techniques in figure 3 for the water map (left graph) and the iodine map (right graph). These results were assessed following the application of a ring artifact correction. In Figure I of the supplemental material, the same results were obtained both before and after the correction in the iodine map for a subset of the data points presented in Figure 3. This demonstrates that the correction equally

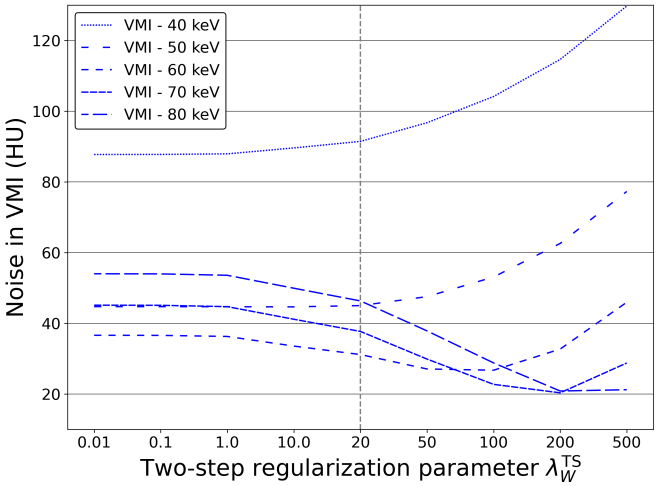

Figure 4. Noise in the iodine insert for VMIs computed at 40, 50, 60, 70 and 80 keV for different two-step water regularization parameters λ_W^{TS}. The iodine regularization parameter was kept constant $\lambda_I^{\mathrm{TS}} = 100$. The gray line represents the selected water regularization parameter $\lambda_W^{\mathrm{TS}} = 20$.

impacts two-step and one-step images at identical noise and spatial resolution levels. Each point displayed in figure 3 represents a reconstruction characterized by one or two regularization parameters for the two-step and one-step methods, respectively. It is visible that one-step reconstruction has the potential to improve spatial resolution for the same noise level as two-step reconstruction, or that it can decrease the noise at the same $f_{\mathrm{TTF10\%}}$ value. As the targeted clinical task is the lumen vessel visualization, the trade-off is more visible in the iodine map and the measured spatial frequency is smaller in the water map. For the smallest regularization levels ($\lambda_{\mathrm{I}}^{\mathrm{OS}} \in [1, 3000]$), one-step reconstruction reduces more the noise in the water map for the same resolution loss compared to the two-step method (i.e. the curve slope is steeper in this region). The $f_{\mathrm{TTF10\%}}$ evaluated in the water map are smaller because of the lower amount of contrast present in this material map (cf figure 2).

It is also visible that the water and iodine regularization weights of one-step reconstruction are linked: the iodine image quality improves when increasing the regularization of water by increasing $\lambda_{\mathrm{W}}^{\mathrm{OS}}$. However, a too strong regularization difference between the water and iodine weights is not recommended because it can lead to a cross-talk effect. For example, for the one-step cases with $\lambda_{\mathrm{I}}^{\mathrm{OS}} = 4000$ (see dashed black curve in figure 3 right), the noise is decreased from $\lambda_{\mathrm{W}}^{\mathrm{OS}} = 0.0$ to $\lambda_{\mathrm{W}}^{\mathrm{OS}} = 0.1$ but is then increased for higher values of $\lambda_{\mathrm{W}}^{\mathrm{OS}}$. The cross-talk also negatively impacts the water map (left graph) with a loss of spatial resolution for a high water parameter ($\lambda_{\mathrm{W}}^{\mathrm{OS}} = 2.0$) compared to the same iodine regularization levels at lower water parameter values. Two cases with a large weight difference are shown in supplemental material figure IIIa and figure IIIb.

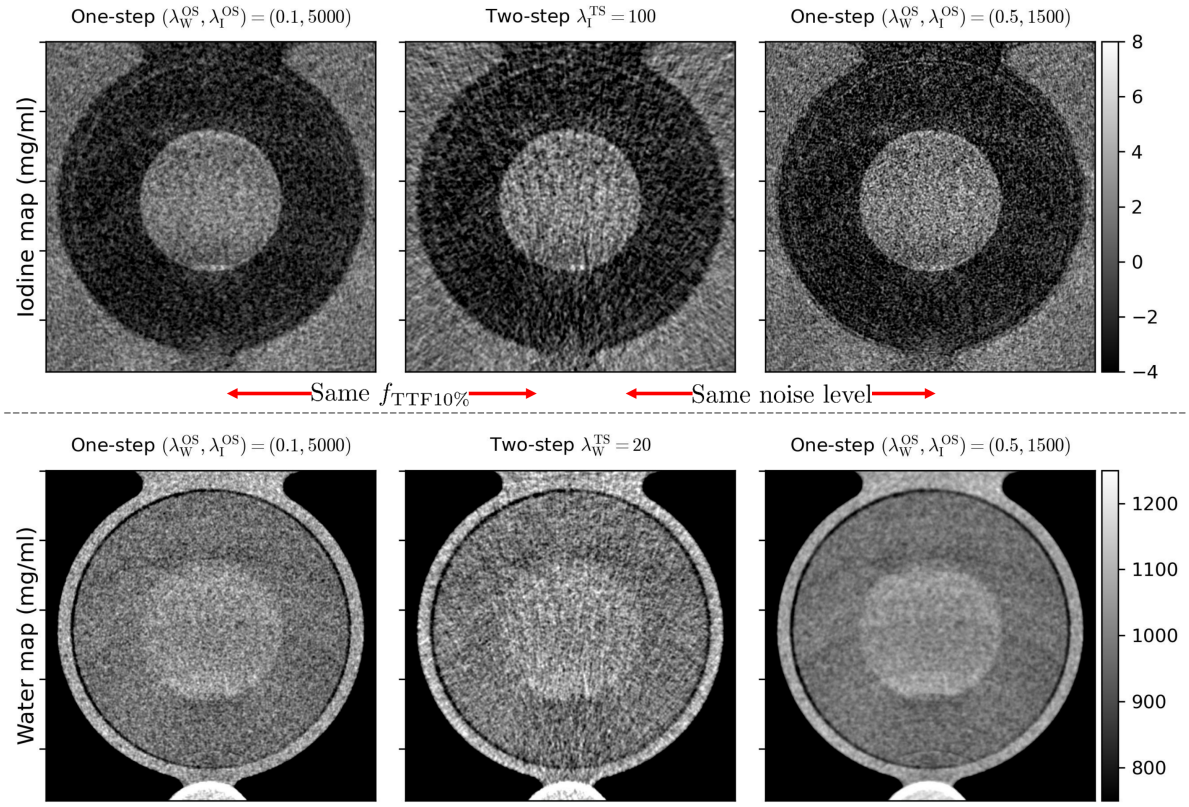

Figure 5. Iodine and water maps of the insert for three different reconstructions: a two-step case in the middle, a one-step case at the same resolution in the iodine map on the left and the same noise level in the iodine map on the right. The water maps do not have matching noise or spatial resolution. Theses cases correspond to the values framed in figure 3.

For the CTA clinical task, the water map is not directly read by the radiologist. However, it impacts the VMI that will be read. In order to select the water regularization parameter in the two-step method, the noise was measured in the VMIs. The parameter $\lambda_I^{\mathrm{TS}} = 100$ corresponds to the noise reduction level of the clinical protocol. For this parameter, the noise in the iodine insert in the VMIs is displayed in figure 4 as a function of the water regularization parameter λ_W^{TS}. The behaviour is different depending on the energy: for the lowest energies (40 and 50 keV), the noise increases with the water regularization parameter. At other energies (60, 70 and 80 keV), the noise starts by decreasing when the water parameter increases before increasing at the highest values. In the CTA clinical task, the VMIs at the lowest energies are critical because of the iodine signal. The water regularization parameter value $\lambda_W^{\mathrm{TS}} = 20$ is a trade-off between limiting the noise at 40 and 50 keV while providing a noise reduction at 60, 70 and 80 keV.

3.3. Comparison of the three selected phantom cases

The cases framed in figure 3 have been selected for further comparison: a two-step case with a regularization level of $\lambda_{\mathrm{I}}^{\mathrm{TS}}$ of 100 and two one-step cases corresponding to the

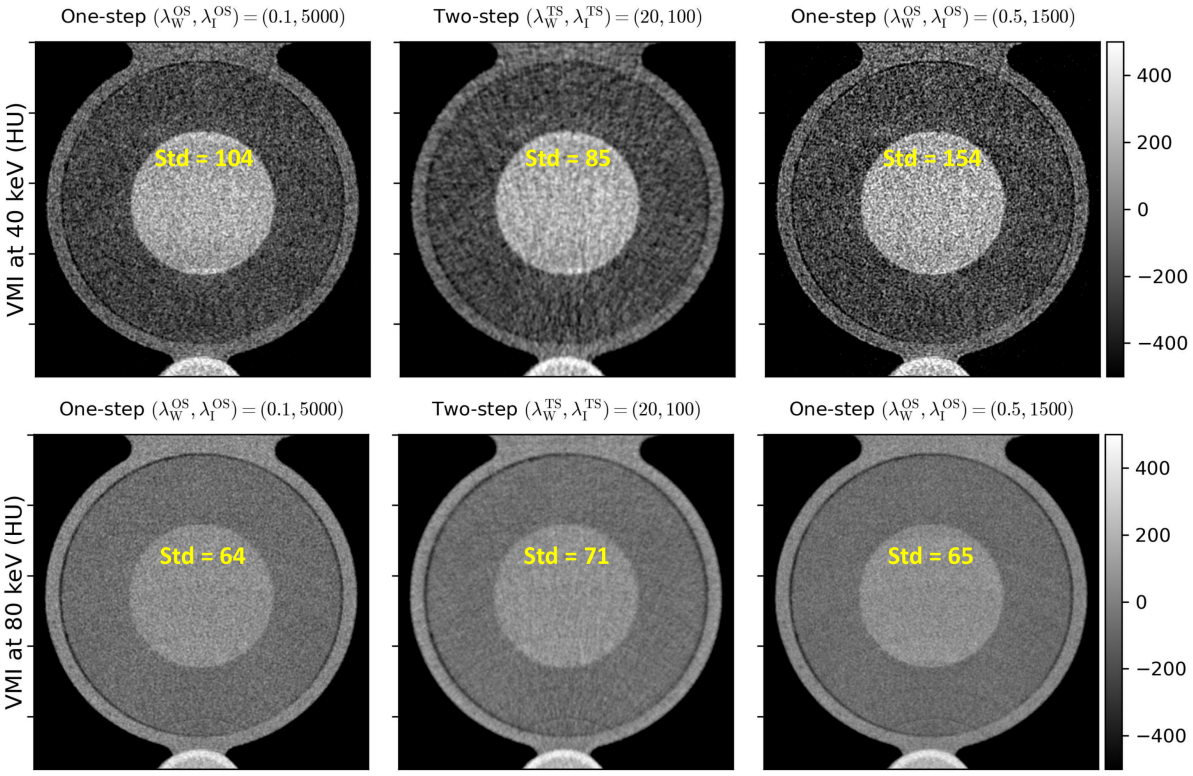

Figure 6. VMIs computed at 40 and 80 keV for the three selected cases displayed in figure 5. The values displayed in yellow are the noise values (HU) evaluated in the iodine insert.

same noise and spatial resolution, with regularization weights $(\lambda_W^{OS}, \lambda_I^{OS})$ of $(0.5, 1500)$ and $(0.1, 5000)$, respectively. The highest water regularization levels were not selected for comparison because the cross talk effect between materials discussed above was visible.

The water and iodine maps corresponding to these three cases are displayed in figure 5. The different noise textures are visible. The one-step reconstruction displays a finer noise texture enabling a lower noise level for the same resolution or an improved resolution at the same noise level. In the water volumes, the contrast is less visible but differences are visible in the noise textures.

For the patient analysis, the radiologist has evaluated the imaging and diagnostic scores on the iodine map and the VMIs. The 40 and 80 keV VMIs are displayed in figure 6 for the three selected cases. The differences between the two techniques are greater at 40 keV where the iodine map has a higher weight. Even if the one-step images have been computed with regularization parameters leading to lower noise levels in the water/iodine MD, the resulting noise is smaller in the VMIs at 40 keV and the noise texture is finer.

The NPS of the iodine maps was calculated to evaluate the noise texture. The NPS is plotted in the left panel of figure 7. When the noise is at a similar level (i.e. same area under the curve), the one-step method better preserves high frequencies than

the two-step method. This translates into a higher NPS in the high-frequency region. Increasing the regularization will lead to the case at matching $f_{\text{TTF10\%}}$, where the high frequencies are similar to the two-step method but low-frequencies are reduced in the one-step iodine map. This quantitatively illustrates differences in noise texture with finer details better preserved by the one-step algorithm, as observed in the iodine maps in figure 5 (top row).

Finally, the TTF are presented in the right panel of figure 7. The reconstructed images with the same spatial resolution have similar curves. However, the one-step reconstruction matching the two-step noise level has an improved TTF.

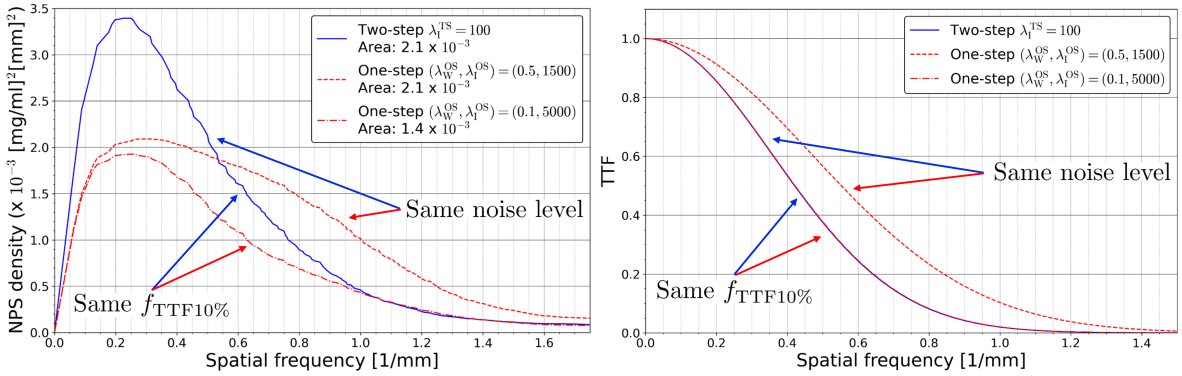

Figure 7. Left: NPS evaluated for the three selected cases of figure 5. The area under the curves are indicated in the legend. These areas measure the noise level. Right: Task transfer functions (TTFs) curves for the three selected cases. These curves were evaluated in the iodine maps.

3.4. Patient imaging scores

The parameters selected for the patient analysis based on the phantom results were $(\lambda_I^{\text{TS}}, \lambda_W^{\text{TS}}) = (100, 20)$ for the two-step algorithm. These parameters lead to a noise level similar to the clinical protocol in the iodine map and a trade-off between VMIs at different energies (figure 6). For the one-step algorithm, the selected parameters were $(\lambda_I^{\text{OS}}, \lambda_W^{\text{OS}}) = (0.1, 5000)$. These values match the spatial resolution of the iodine map of the two-step method (figure 3) without visual cross-talk effect. The resulting images are displayed in figure 8.

The contrast level in a VMI depends on the computed energy and increases when the energy decreases (figure 8). VMI at low energies have already demonstrated enhancement of the vessel lumen and potential reduction of contrast administration (McCollough *et al.* 2020). As a result, the VMI at 40, 50 and 60 keV presented the greatest score for the two-step method.

The mean score of the iodine image overall quality was 1.7 ± 0.5 and 4.2 ± 0.9 for the two-step and one-step algorithms, respectively (figure 9). The iodine image score for the implemented two-step algorithm was below the threshold for clinical use in all cases. However, the VMIs computed from these iodine images present closer evaluations

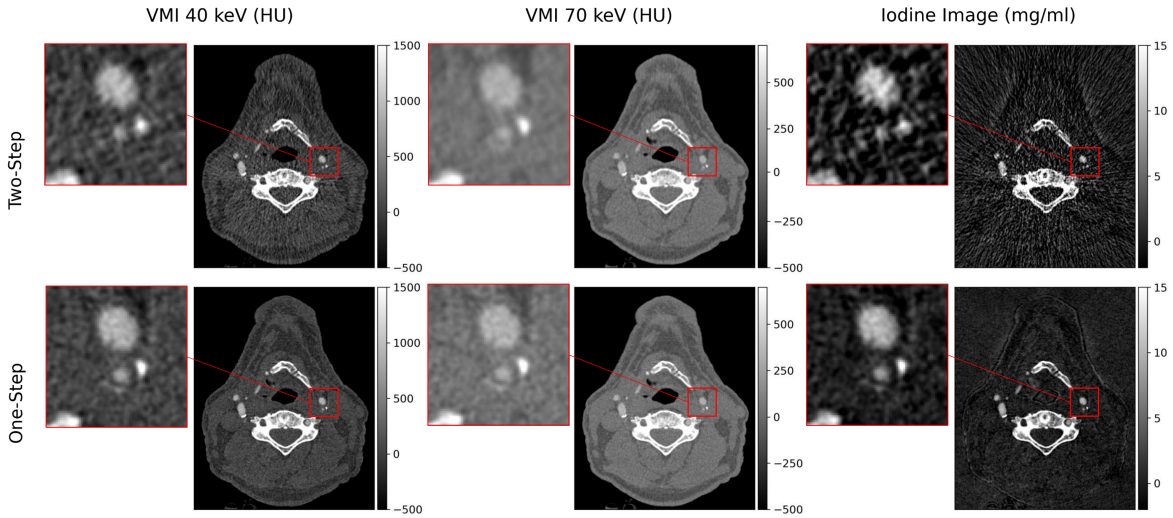

Figure 8. Example case of a carotid spectral photon-counting CT angiography in a 68-years-old man using VMIs at 40 keV and 70 keV and iodine images. The one-step spectral images enable a better depiction of a severe carotid stenosis associated with a calcified plaque in comparison to the two-step images (zoomed areas).

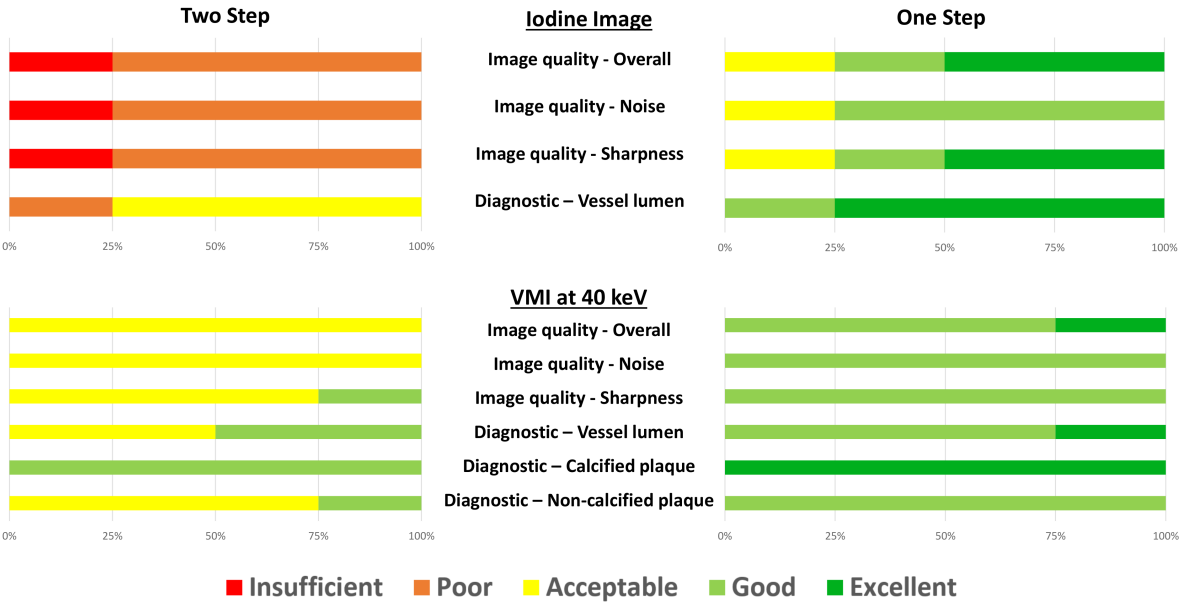

Figure 9. Detailed image quality and diagnostic scores for the iodine images and VMIs for the two-step method (left) and one-step (right) methods.

with a mean score of 3.3 ± 0.5 for the two-step method and 4.4 ± 0.5 for the one-step method (averaged over all VMIs). This indicates that the VMIs are above the acceptable threshold even if the iodine image is not.

Similar observations of the noise scores were made for the iodine image with a mean score of 1.7 ± 0.5 (two-step) and 3.7 ± 0.5 (one-step) compared to a mean VMI score of 2.9 ± 0.2 (two-step) and 4.0 ± 0.0 (one-step). For the sharpness score, the levels in the iodine image were 1.7 ± 0.5 (two-step) and 4.2 ± 0.9 (one-step) and, averaged over

all VMIs, 3.2 ± 0.4 (two-step) and 4.0 ± 0.0 (one-step).

The percentages of patients with a score improvement are displayed in table 3. The one-step method has improved the image quality criteria in all images. This led to an improvement of diagnostic task scores in most cases except at lower VMI energies (40, 50 and 60 keV) were the two-step method provided acceptable to good scores for one patient.

Table 3. Percentages of patient with a score improvement with the one-step method compared to the two-step method. N/A: Non Available, only the vessel lumen clinical task was evaluated in iodine maps.

Criterion	40 keV	50 keV	60 keV	70 keV	80 keV	Iodine
Image quality - Overall	100%	100%	100%	100%	100%	100%
Image quality - Noise	100%	100%	100%	100%	100%	100%
Image quality - Sharpness	100%	100%	100%	100%	100%	100%
Diagnostic - Vessel lumen	75%	75%	75%	100%	100%	100%
Diagnostic - Calcified plaque	100%	100%	100%	100%	100%	N/A
Diagnostic - Non-calcified plaque	75%	75%	75%	75%	75%	N/A

4. Discussion

The evaluation of phantom data has shown that the one-step method can improve image quality compared to the selected two-step method even with the same spatial regularizer. The one-step algorithm can either provide a better spatial resolution at the same noise level or a lower noise level at the same spatial resolution in the material decomposed images. The NPS curves in section 3.3 illustrate that the one-step method preserves the high spatial frequencies for the same noise level. However, the one-step algorithm requires a longer computation time.

Indeed, the selected two-step algorithm operates the MD on a pixel-by-pixel basis which is very efficient regarding computation time. More sophisticated methods could have been used, e.g. with a regularization term on the sinograms or using a joint reconstruction of the decomposed basis material sinograms. This would have increased the computation time and/or the number of parameters to tune and the focus of this work was the comparison with a two-step reconstruction algorithm with a similar spatial regularization term. One limitation of this comparison lies in the absence of

a dedicated evaluation of ring artifacts, which might differ between the two-step and one-step strategies. In this study, a post-processing ring artifact correction was applied to both approaches. However, further ring corrections could be investigated but would be specific to each method. For example, the one-step scheme could be improved with the modification of the spectral model (Eq. 2) to correct for ring artifacts during the reconstruction process (Schmidt *et al.* 2017). Figure 3 illustrates how a one-step scheme has the ability to reduce noise while preserving spatial resolution. On clinical spectral CTs, the selected two-step scheme is coupled with image post-processing to improve image quality which could also be applied to one-step images.

Because the computation time of the one-step implementation was not optimized, we do not provide the computation time of the two techniques but the one-step algorithm is significantly more computationally demanding than the two-step algorithm. A limitation of the current work is that the implemented two-step algorithm is different from the clinical two-step algorithm. Indeed, the reconstruction algorithm is a model-based technique which, to our knowledge, is not currently employed in clinical scanners. Another limitation is the difference in noise texture compared to FBP images. This would modify the NPS curves presented in figure 7. FBP images are also characterized by streak artifacts whereas model-based reconstructions will present patchy images with strong spatial regularization.

For the one-step method, the quantitative measurements of the phantom images have demonstrated how the regularization level applied to a material map can impact the other basis material map. The choice of regularization parameters is more complicated to avoid this cross-talk effect between material maps and it can impact both spatial resolution at an edge between two materials and the spectral separation between the two material density maps. The cross-talk impact could be further studied with other iodine concentrations. The clinical analysis was not made on the reconstructed water volume. However, the latter has an impact on the reconstructed VMIs. This impact is different for the two-step or the one-step method. The pre-reconstruction MD two-step methods provide an anti-correlated noise between the water and iodine maps (Persson and Grönberg 2017). Indeed, for the regularization parameters applied to the patient data, the Pearson correlation coefficients were -0.91 and -0.13 for the two-step and the one-step methods, respectively. The two-step maps have a stronger covariance with anti-correlated noise and these noise properties will have different impact depending on the VMI computation (Leng *et al.* 2015) (see figure 4). This complicates the comparison of the two techniques on VMIs as regularization parameters that lead to similar properties in material maps would lead to different VMI noise properties. This means that there is not an optimal set of parameters leading to a fair comparison of VMIs at all energies for the two techniques. The choice has been made in this study to focus on the iodine map comparison (cf figure 3), as this map is a direct result of the MD problem.

The phantom data were acquired at a conventional dose for clinical CT. The quantitative results could vary and the difference between the one-step and the two-step methods may be even larger at lower dose or at a smaller iodine concentration

in the CTA insert. The scanner was operated with a 2×2 binning, which provides a slightly smaller detector pixel size at the isocenter (0.55 mm) compared to average commercial DE-CTs (0.6-0.75 mm). The results of this study indicate that the one-step algorithm could reconstruct spectral images at the full PCD-CT spatial resolution and low-dose. New CTA protocols are also investigated with the injection of K-edge contrast agents (Si-Mohamed *et al.* 2021a). This would require a three-material basis MD with a potential noise increase which might be better mitigated with the one-step method than with the two-step method.

The clinical purpose of CTA protocols is the depiction of the calcified plaques around the carotid artery (see supplemental figure I). This protocol benefits from an increased spatial resolution and the patient data were acquired with a low-dose protocol. In this context, the one-step algorithm presented a good overall image quality score in the iodine maps. This shows that the one-step method can enable spectral reconstruction at a low irradiation dose. The VMIs reconstructed with the selected two-step method take advantage of the correlated noise in the iodine and water maps and present at some energy an acceptable image quality. The VMIs computed with the one-step method still had higher image quality and diagnostic scores.

The phantom used in this work was specifically designed to reproduce the CTA diagnostic task. The impact of the regularization parameters would be different for a different task. Moreover, the basis materials choice (iodine and water) depends on the clinical task and would be different. For example, a calcium and water basis would be selected in the absence of a contrast agent injection or the photo-electric and compton energy functions to evaluate the atomic number. Nevertheless, the image quality metrics measured on the phantom acquisitions presented a correlation with the scores evaluated by an experienced radiologist. This correlation could be extended from the evaluated NPS and TTF properties to other clinical tasks. A detectability index associated to a model observer could be computed (Rotzinger *et al.* 2021; Solomon *et al.* 2015) to further investigate the correlation between these metrics and the radiologist scores in a study including more patients and several radiologists. The presented phantom methodology is relevant to compare spectral imaging algorithms and set the regularization weights of the iterative reconstruction methods to, eventually, improve image quality in patient studies.

5. Conclusions

The presented one-step method improved image quality compared to a reference two-step algorithm. The noise and spatial resolution improvements were measured on phantom data designed for the CTA clinical task. This translated into higher image quality and diagnostic scores evaluated by a radiologist on patient images. This demonstrates that the one-step method can be used at low doses to reconstruct spectral CT images with a high spatial resolution while maintaining a low noise level.

Acknowledgments

We thank David C. Rotzinger, Damien Racine, Fabio Becce for the CTA insert design and availability, Valérie Leitman, Angéle Houmeau, Morgane Bouin, Apolline Barbe, Adeline Mansuy for their support on the clinical protocol with patients, Mohammad Varasteh, Thomas Broussaud for their help with the image acquisition, Sara Boccalini, Riham Dessouky for their clinical insight on CTA, Yoad Yagil, Klaus Erhard, Heiner Daerr, Elias Lahoud for the data exportation and calibration routines. This work was performed within the framework of the SIRIC LYriCAN Grant INCa-INSERM-DGOS-12563 and the LABEX PRIMES (ANR-11-LABX-0063) of Université de Lyon, within the program "Investissements d'Avenir" (ANR-11-IDEX-0007) operated by the ANR.

Ethical Statement

This work involves human participants. This prospective institutional review board–approved study was conducted at a cardiothoracic university hospital (Hôpital Louis Pradel, Hospices Civils de Lyon, France) from January to June 2021 (Ethics committee: Hospices Civils de Lyon, approval number: 2019-A02945–52).

The authors declare that the work described has been carried out in accordance with the Declaration of Helsinki of the World Medical Association revised in 2013 for experiments involving humans. The authors declare that this report does not contain any personal information that could lead to the identification of the patients. The authors declare that a written informed consent has been signed by each participant included in this work.

References

Alvarez, Robert and Albert Macovski (1976). "Energy-selective reconstructions in X-ray computerized tomography". In: *Physics in Medicine and Biology* 21.5, pp. 733–744.

Barber, Rina Foygel *et al.* (2016). "An algorithm for constrained one-step inversion of spectral CT data". In: *Physics in Medicine & Biology* 61 (10), p. 3784.

Boccalini, Sara *et al.* (2021). "Feasibility of human vascular imaging of the neck with a large field-of-view spectral photon-counting CT system". In: *Diagnostic and Interventional Imaging* 102.5, pp. 329–332. ISSN: 2211-5684. DOI: https://doi.org/10.1016/j.diii.2020.12.004. URL: https://www.sciencedirect.com/science/article/pii/S2211568420303235.

Cai, C. *et al.* (2013). "A full-spectral Bayesian reconstruction approach based on the material decomposition model applied in dual-energy computed tomography". In: *Medical Physics* 40.11, p. 111916. DOI: https://doi.org/10.1118/1.4820478. eprint: https://aapm.onlinelibrary.wiley.com/doi/pdf/10.1118/1.4820478. URL: https://aapm.onlinelibrary.wiley.com/doi/abs/10.1118/1.4820478.

Chen, Buxin *et al.* (2021). "Non-convex primal-dual algorithm for image reconstruction in spectral CT". In: *Computerized Medical Imaging and Graphics* 87, p. 101821.

Danielsson, Mats *et al.* (Feb. 2021). *Photon-counting x-ray detectors for CT*. DOI: 10.1088/1361-6560/abc5a5.

Feng, Mang *et al.* (Aug. 2021). "An experimental method to correct low-frequency concentric artifacts in photon counting CT". In: *Physics in Medicine and Biology* 66.17, p. 175011. DOI: 10.1088/1361-6560/ac1833. URL: https://dx.doi.org/10.1088/1361-6560/ac1833.

Flohr, Thomas *et al.* (Nov. 2020). "Photon-counting CT review". In: *Physica Medica* 79, pp. 126–136. ISSN: 11201797. DOI: 10.1016/j.ejmp.2020.10.030.

Green, P.J. (1990). "Bayesian reconstructions from emission tomography data using a modified EM algorithm". In: *IEEE Transactions on Medical Imaging* 9.1, pp. 84–93. DOI: 10.1109/42.52985.

Hudson, H.M. and R.S. Larkin (1994). "Accelerated image reconstruction using ordered subsets of projection data". In: *IEEE Transactions on Medical Imaging* 13.4, pp. 601–609. DOI: 10.1109/42.363108.

Jolivet, Frédéric *et al.* (2020). "An efficient one-step method for spectral CT based on an approximate linear model". In: *IEEE Transactions on Radiation and Plasma Medical Sciences* 5 (4), pp. 528–536.

Lee, Donghyeon *et al.* (2022). "A generalized simultaneous algebraic reconstruction technique (GSART) for dual-energy X-ray computed tomography". In: *Journal of X-Ray Science and Technology* (Preprint), pp. 1–18.

Leipsic, Jonathon *et al.* (Sept. 2014). "SCCT guidelines for the interpretation and reporting of coronary CT angiography: A report of the Society of Cardiovascular Computed Tomography Guidelines Committee". In: *Journal of Cardiovascular Computed Tomography* 8 (5), pp. 342–358. ISSN: 1876861X. DOI: 10.1016/j.jcct.2014.07.003.

Leng, Shuai *et al.* (2015). "Maximizing Iodine Contrast-to-Noise Ratios in Abdominal CT Imaging through Use of Energy Domain Noise Reduction and Virtual Monoenergetic Dual-Energy CT". In: *Radiology* 276.2. PMID: 25860839, pp. 562–570. DOI: 10.1148/radiol.2015140857.

Liu, Stephen Z *et al.* (2022). "Model-based three-material decomposition in dual-energy CT using the volume conservation constraint". In: *Physics in Medicine & Biology* 67 (14), p. 145006.

Long, Yong and Jeffrey A Fessler (2014). "Multi-material decomposition using statistical image reconstruction for spectral CT". In: *IEEE transactions on medical imaging* 33 (8), pp. 1614–1626.

Maaß, Clemens *et al.* (2009). "Image-based dual energy CT using optimized precorrection functions: A practical new approach of material decomposition in image domain". In: *Medical Physics* 36.8, pp. 3818–3829. DOI: https://doi.org/10.1118/1.3157235. eprint: https://aapm.onlinelibrary.wiley.com/doi/

pdf/10.1118/1.3157235. URL: https://aapm.onlinelibrary.wiley.com/doi/abs/10.1118/1.3157235.

McCollough, Cynthia H *et al.* (2020). "Principles and applications of multienergy CT: Report of AAPM Task Group 291". In: *Medical physics* 47 (7), e881–e912.

Mechlem, Korbinian *et al.* (2017). "Joint statistical iterative material image reconstruction for spectral computed tomography using a semi-empirical forward model". In: *IEEE transactions on medical imaging* 37 (1), pp. 68–80.

Si-Mohamed, Salim *et al.* (July 2021a). "In Vivo Molecular K-Edge Imaging of Atherosclerotic Plaque Using Photon-counting CT". In: *Radiology* 300 (1), pp. 98–107. ISSN: 15271315. DOI: 10.1148/radiol.2021203968.

Si-Mohamed, Salim *et al.* (2021b). "Spectral Photon-Counting CT Technology in Chest Imaging". In: *Journal of Clinical Medicine* 10.24. ISSN: 2077-0383. DOI: 10.3390/jcm10245757. URL: https://www.mdpi.com/2077-0383/10/24/5757.

Si-Mohamed, Salim *et al.* (2022). "Coronary CT Angiography with Photon-counting CT: First-In-Human Results". In: *Radiology* 303.2. PMID: 35166583, pp. 303–313. DOI: 10.1148/radiol.211780.

Si-Mohamed, Salim A *et al.* (2023). "First Experience With a Whole-Body Spectral Photon-Counting CT Clinical Prototype". In: DOI: 10.1097/RLI.0000000000000965. URL: www.investigativeradiology.com.

Mory, Cyril *et al.* (2018). "Comparison of five one-step reconstruction algorithms for spectral CT". In: *Physics in Medicine & Biology* 63 (23), p. 235001.

Nelder, J. A. and R. Mead (Jan. 1965). "A Simplex Method for Function Minimization". In: *The Computer Journal* 7.4, pp. 308–313. ISSN: 0010-4620. DOI: 10.1093/comjnl/7.4.308. eprint: https://academic.oup.com/comjnl/article-pdf/7/4/308/1013182/7-4-308.pdf. URL: https://doi.org/10.1093/comjnl/7.4.308.

Nesterov, Yu (May 2005). "Smooth minimization of non-smooth functions". In: *Mathematical Programming* 103 (1), pp. 127–152. ISSN: 0025-5610. DOI: 10.1007/s10107-004-0552-5.

Nocedal (2006). *Numerical Optimization*. Springer New York. ISBN: 978-0-387-30303-1. DOI: 10.1007/978-0-387-40065-5.

Persson, Mats and Fredrik Grönberg (2017). "Bias–variance tradeoff in anticorrelated noise reduction for spectral CT". In: *Medical Physics* 44.9, e242–e254. DOI: https://doi.org/10.1002/mp.12322. eprint: https://aapm.onlinelibrary.wiley.com/doi/pdf/10.1002/mp.12322. URL: https://aapm.onlinelibrary.wiley.com/doi/abs/10.1002/mp.12322.

Rajendran, Kishore *et al.* (Oct. 2021). "Full field-of-view, high-resolution, photon-counting detector CT: Technical assessment and initial patient experience". In: *Physics in Medicine and Biology* 66 (20). ISSN: 13616560. DOI: 10.1088/1361-6560/ac155e.

Richard, S. *et al.* (July 2012). "Towards task-based assessment of CT performance: system and object MTF across different reconstruction algorithms". In: *Med Phys* 39 (7), pp. 4115–4122. ISSN: 0094-2405. DOI: 10.1118/1.4725171.

Rit, Simon *et al.* (2014). "The Reconstruction Toolkit (RTK), an open-source cone-beam CT reconstruction toolkit based on the Insight Toolkit (ITK)". In: *Journal of Physics: Conference Series* 489 (1), p. 12079.

Rodesch, Pierre-Antoine *et al.* (2020). "Spatially varying regularization weights for one-step spectral CT with SQS". In: *Sixth international conference on image formation in X-ray computed tomography*, pp. 58–61.

Roessl, E and R Proksa (July 2007). "K-edge imaging in x-ray computed tomography using multi-bin photon counting detectors". In: *Physics in Medicine & Biology* 52.15, p. 4679. DOI: 10.1088/0031-9155/52/15/020. URL: https://dx.doi.org/10.1088/0031-9155/52/15/020.

Rotzinger, David *et al.* (2021). "Performance of spectral photon-counting coronary CT angiography and comparison with energy-integrating-detector CT: objective assessment with model observer". In: *Diagnostics* 11 (12), p. 2376.

Samei, Ehsan *et al.* (2019). "Performance evaluation of computed tomography systems: summary of AAPM task group 233". In: *Medical physics* 46 (11), e735–e756.

Schmidt, Taly Gilat *et al.* (2017). "A Spectral CT Method to Directly Estimate Basis Material Maps From experimental Photon-Counting Data". In: *IEEE Transactions on Medical Imaging* 36.9, pp. 1808–1819. DOI: 10.1109/TMI.2017.2696338.

Schmidt, Taly Gilat *et al.* (2022). "Addressing CT metal artifacts using photon-counting detectors and one-step spectral CT image reconstruction". In: *Medical Physics* 49.5, pp. 3021–3040. DOI: https://doi.org/10.1002/mp.15621. eprint: https://aapm.onlinelibrary.wiley.com/doi/pdf/10.1002/mp.15621. URL: https://aapm.onlinelibrary.wiley.com/doi/abs/10.1002/mp.15621.

Simard, Mikaël and Hugo Bouchard (2022). "One-step iterative reconstruction approach based on eigentissue decomposition for spectral photon-counting computed tomography". In: *Journal of Medical Imaging* 9.4, p. 044003. DOI: 10.1117/1.JMI.9.4.044003. URL: https://doi.org/10.1117/1.JMI.9.4.044003.

Solomon, Justin *et al.* (2015). "Diagnostic Performance of an Advanced Modeled Iterative Reconstruction Algorithm for Low-Contrast Detectability with a Third-Generation Dual-Source Multidetector CT Scanner: Potential for Radiation Dose Reduction in a Multireader Study". In: *Radiology* 275.3. PMID: 25751228, pp. 735–745. DOI: 10.1148/radiol.15142005. eprint: https://doi.org/10.1148/radiol.15142005. URL: https://doi.org/10.1148/radiol.15142005.

Tairi, Souhil *et al.* (2020). "ProMeSCT: A Proximal Metric Algorithm for Spectral CT". In: *IEEE Transactions on Radiation and Plasma Medical Sciences* 5 (4), pp. 548–558.

Tilley, Steven *et al.* (Jan. 2019). "Model-based material decomposition with a penalized nonlinear least-squares CT reconstruction algorithm". In: *Physics in Medicine &*

Biology 64.3, p. 035005. DOI: 10.1088/1361-6560/aaf973. URL: https://dx.doi.org/10.1088/1361-6560/aaf973.

Weidinger, Thomas *et al.* (2016). "Polychromatic iterative statistical material image reconstruction for photon-counting computed tomography". In: *International journal of biomedical imaging* 2016.

Weigold, Wm Guy *et al.* (May 2011). "Standardized medical terminology for cardiac computed tomography: A report of the Society of Cardiovascular Computed Tomography". In: *Journal of Cardiovascular Computed Tomography* 5 (3), pp. 136–144. ISSN: 19345925. DOI: 10.1016/j.jcct.2011.04.004.